Dual-Continuum Models of Lithium-Ion Batteries are Fast and Accurate Alternatives to the Doyle-Fuller-Newman Approach: I. Derivation and Validation

Isaac B Paten, Martin Petitfrére, Céline Merlet, Romain de Loubens, Michel Quintard, Yohan Davit

Journal of The Electrochemical Society, 2026 **173** 030503

Dual-Continuum Models of Lithium-Ion Batteries are Fast and Accurate Alternatives to the Doyle-Fuller-Newman Approach: I. Derivation and Validation

Isaac B. Paten,[1] Martin Petitfrére,[2] Céline Merlet,[3,4] Romain De Loubens,[2] Michel Quintard,[1] and Yohan Davit[1,z]

[1] *Institut de Mécanique des Fluides de Toulouse (IMFT, UMR 5502), Université de Toulouse, CNRS, INPT, UPS, 31400 Toulouse, France*
[2] *TotalEnergies–OneTech, 91120 Palaiseau, France*
[3] *CIRIMAT, Université de Toulouse, INPT, CNRS, 31062 Toulouse, France*
[4] *Réseau sur le Stockage Électrochimique de l'Énergie (RS2E), Fédération de Recherche CNRS 3459, 80039 Amiens, France*

One of the main reasons for the Doyle–Fuller–Newman (DFN) model's success in simulating lithium-ion batteries is also one of its main limitations—its hybrid micro/macro formulation. On one hand, this captures the slow diffusion of lithium within the active material particles. On the other hand, it makes the retention of realistic particle geometries computationally prohibitive, thereby provoking strongly simplifying assumptions on their shape. Dual-continuum models employ a fully macroscale description of the battery, and thus can potentially circumvent these challenges. Despite their widespread use in other fields, they have seen little application in battery modelling. In this work, we derive a dual-continuum model for lithium-ion batteries using the volume-averaging technique. A novel mapping between the volume-averaged and surface-averaged active material concentrations is introduced, based on the microscale source terms that generate concentration fluctuations. Unlike the DFN model, this approach makes no assumptions about particle shape but instead relies on a closure problem solved on the electrode microstructure. The resulting model is validated against a detailed microscale model, the DFN model, a recent dual-continuum formulation, and experimental data. Across all cases considered, our dual-continuum model reproduced cell-voltage data more accurately than the DFN approach while requiring 70–80% less computation time.

 [DOI: 10.1149/1945-7111/ae335f]

Manuscript submitted October 13, 2025; revised manuscript received December 11, 2025. Published January 30, 2026.

Supplementary material for this article is available online

The Doyle–Fuller–Newman (DFN) model is considered the industrial and academic standard for physics-based modelling of lithium-ion batteries at the cell scale, and has prevailed now for about 30 years.[1] One can find it referred to under various other names—the Newman model, porous electrode theory, P2D, etc.—and various extensions or simplifications of the original model have come about since its inception.[2–5] From the perspective of upscaling theories,[6,7] the DFN can be considered a *hybrid* model,[8] since all transport equations are solved on the macroscale, except the mass balance within the active material (AM), which is solved on the microscale. This hybrid micro/macro formulation is one of the key strengths of the DFN, as it captures the slow transport of lithium within the AM and thus allows an accurate estimate of surface concentration for use in the Butler-Volmer (BV) Equation.

Although the DFN model has found tremendous success, adopting a hybrid approach comes with drawbacks. One is strongly compelled to make some simplifying assumptions on the morphology of the microscale domain to reduce computational cost. In theory, the full complexity of the microstructure can be kept in a hybrid model (see the "homogenised model" in Brosa-Planella's review[9]), but the resulting calculation will be almost as computationally expensive as the direct numerical simulation (DNS); we use the term DNS here in the sense found in the volume-averaging literature,[10,11] to refer to the solution of microscale model (described below) on the entire battery microstructure. In the case of the DFN, the AM particles are almost always assumed to be isolated spheres. Evidently, this is a strong assumption, and the geometry of real battery electrodes may be far from this ideal case. In tandem with the assumption that all variables do not vary over the surface of these spheres, the concentration field becomes spherically symmetric, allowing the AM mass conservation equation to be solved in 1D along the particle radius—when coupled with a single macroscale dimension along the electrode thickness, this gives rise to the ubiquitous "pseudo 2-dimensional" case. Despite these simplifications, the DFN remains too computationally expensive for certain applications, such as battery management systems,[12] thus motivating a large research effort to develop lighter models. These include several variants of the Single Particle Model (SPM),[2,3,13] attempts to approximate the concentration profile within AM particles to avoid numerically solving a partial-differential equation (PDE),[4,5,14–22] or further reduction to a phenomenological equivalent-circuit model.[9,23] Therefore, an interesting alternative to the DFN would be a model that improves its accuracy and/or reduces computational cost.

Amongst the vast upscaling literature, another family of models can be found alongside the hybrid approach: "dual-continuum" (DC) models. These offer a fully-macroscale description of the problem, and thus do not require solution on a microscale domain, reducing computational load relative to a hybrid model. They can be found under various names, such as multi-equation,[8,24] multi-rate mass transfer[25,26] or dual porosity/region.[27,28] Such models rely on a phase decomposition approach, where each 'continuum' describes the behaviour of intrinsic phase averages, and they are coupled via exchange terms—here, we are specifically interested in one phase for the electrolyte and one for the AM.

Although DC models have proven effective in a wide range of applications, such as heat-transfer[24] and petroleum engineering,[29–31] they have scarcely appeared in the battery-modelling literature. To the best of the authors' knowledge, only two instances can be found.[28,32] The first instance of a DC model for Li-ion batteries was presented by Arunachalam and Onori.[32] The authors showed that their model outperforms the DFN in certain conditions, such as at high temperatures. They used the intrinsic *volume average* of lithium concentration within the AM particles, $\langle c_k \rangle^k$, for calculating the reaction rate via the BV equation (where $k \in \{n, p\}$, denoting the concentration in either the negative or positive electrode). However, in many cases, the volume averaged concentration may be far from the surface-averaged concentration, $\langle c_k \rangle_A$, thus yielding a poor

[z] E-mail: yohan.davit@imft.fr

estimate of reaction rate (since reaction takes place at the AM-electrolyte interface). Yang and Tartakovsky[28] improved this model by introducing the concept of a boundary layer in the AM particles and a mapping between $\langle c_k \rangle^k$ and $\langle c_k \rangle_A$. Within the boundary layer, they use a second-order polynomial to describe c_k and thus better approximate the surface concentration. They validated their model by comparison with the DFN and the microscale model on an academic electrode composed of slab-like AM, showing a significant improvement of their DC model compared to the DFN. This scenario is designed to violate the DFN's assumption of spherical particles, thus illustrating one of the strengths of DC models: their ability to describe a broad range of different AM geometries.

In this work, we use the volume-averaging technique (VAT) to develop a DC model, proposing a mapping between $\langle c_k \rangle^k$ and $\langle c_k \rangle_A$ based on the source terms that cause concentration fluctuations on the microscale—this is notably different to Yang's model, as we do not assume the existence of a boundary layer or a polynomial concentration profile, but instead solve a closure problem on microstructure geometry to relate $\langle c_k \rangle^k$ and $\langle c_k \rangle_A$. In Part I of this work, we introduce the theory of the model, then we validate it on several electrodes by comparison with the DNS, DFN, and Yang's model. Finally, we parameterise and validate the model using experimental data. In Part II, several extensions of the model are presented. For the reader unfamiliar with the VAT, it may be preferable to skip to the Model Differences Section initially, so as to first understand the appeal of the model before investing time in the details of its derivation.

Microscale

The reference used to evaluate the DC models and the DFN throughout this work is the numerical solution of the microscale model, herein referred to as the DNS. We consider an electrode composed of two phases, electrolyte and AM, that are at a constant and uniform temperature. The electrolyte domain is denoted as Ω_e, whilst that of the AM as Ω_k, where $k \in \{n, p\}$ to denote the negative or positive electrode respectively. The AM-electrolyte interface is defined as $\partial\Omega_{k,e}$, and the domain encompassing both phases is called $\Omega = \Omega_e \cup \Omega_k$. Overall, two balance equations are required in each phase—a mass and charge balance, each accompanied by a boundary condition (BC) at the internal interface to describe the electrochemical reaction. The system of equations for mass conservation, valid in both the negative and positive electrodes, is summarised below,

$$\partial_t c_e + \nabla\cdot\boldsymbol{N}_e = 0 \qquad \text{in } \Omega_e, \qquad [1a]$$

$$\partial_t c_k + \nabla\cdot\boldsymbol{N}_k = 0 \qquad \text{in } \Omega_k, \qquad [1b]$$

$$\boldsymbol{n}\cdot\boldsymbol{N}_e = F^{-1} j_k \qquad \text{at } \partial\Omega_{k,e}, \qquad [1c]$$

$$\boldsymbol{n}\cdot\boldsymbol{N}_k = F^{-1} j_k \qquad \text{at } \partial\Omega_{k,e}. \qquad [1d]$$

On the other hand, conservation of charge gives,

$$\nabla\cdot\boldsymbol{i}_e = 0 \qquad \text{in } \Omega_e, \qquad [2a]$$

$$\nabla\cdot\boldsymbol{i}_k = 0 \qquad \text{in } \Omega_k, \qquad [2b]$$

$$\boldsymbol{n}\cdot\boldsymbol{i}_e = j_k \qquad \text{at } \partial\Omega_{k,e}, \qquad [2c]$$

$$\boldsymbol{n}\cdot\boldsymbol{i}_k = j_k \qquad \text{at } \partial\Omega_{k,e}, \qquad [2d]$$

where $\boldsymbol{n}$ is the normal vector pointing outwards from the AM domain and F is Faraday's constant. To complete the model above, expressions for $\boldsymbol{N}_e$, $\boldsymbol{N}_k$, $\boldsymbol{i}_e$, $\boldsymbol{i}_k$, and j_k are needed. The electrolyte flux and current density equations are provided by concentrated-solution theory. Mass transport within the AM phase is modelled by Fickian diffusion, and charge transport by Ohm's law,

$$\boldsymbol{N}_e = -D_e \nabla c_e + \frac{t_+^0}{F}\boldsymbol{i}_e, \qquad [3a]$$

$$\boldsymbol{i}_e = -\sigma_e \nabla\phi_e - \sigma_e\theta \nabla \ln c_e, \qquad [3b]$$

$$\boldsymbol{N}_k = -D_k \nabla c_k, \qquad [3c]$$

$$\boldsymbol{i}_k = -\sigma_k \nabla\phi_k, \qquad [3d]$$

where c_e, ϕ_e, D_e, σ_e, and t_+^0 are the electrolyte concentration, potential, diffusivity, conductivity, and transport number (respectively). The AM potential and conductivity are ϕ_k and σ_k respectively, whilst

$$\theta = -\frac{2RT(1 - t_+^0)}{F}(1 + \delta_e), \qquad [4]$$

where R is the gas constant, T is temperature, and $(1 + \delta_e)$ is the thermodynamic factor. Finally, the reaction rate, j_k, is assumed to follow a BV expression,

$$j_k(\phi_e, \phi_k, c_e, c_k) = 2j_{k0}\sinh\left(\frac{F}{2RT}\eta_k\right), \qquad [5]$$

where

$$\eta_k = \phi_k - \phi_e - U_k(c_k), \qquad [6]$$

$$j_{k0} = Fk_k\sqrt{c_k c_e (c_{k,\max} - c_k)}, \qquad [7]$$

and j_{k0} is the exchange current density, η_k is the reaction overpotential, U_k is the open-circuit potential (OCP), k_k is the rate constant, and $c_{k,\max}$ is the maximum concentration of lithium in the AM. Whilst various forms of the expression for j_{k0} can be found in the literature,[9] we have chosen this form since it is common,[33–36] and is the form employed in the sources we use for k_k in the model validation below. The above choices for describing transport and kinetics have become a standard approach to microscale modelling in the literature.[9,34,37–40]

Upscaling the AM Mass Balance Using the VAT

Introduction and definitions.—The DFN consists of 3 macroscale equations—describing mass and charge conservation in the electrolyte, and charge conservation in the AM—completed by a microscale equation, modelling mass transport in the AM. The 3 macroscale equations present in the DFN take an identical form in the DC model developed here, and will therefore be relegated to the supplementary material (SM). The crucial difference between our DC model and the DFN is the homogenisation of the AM phase, presented below. An averaging set centred at position $\boldsymbol{x} \in \Omega$ is defined as $\mathcal{V}(\boldsymbol{x}) \subset \Omega$, whilst the subset of phase γ within this volume is $\mathcal{V}_\gamma(\boldsymbol{x}) \subset \mathcal{V}(\boldsymbol{x})$. Phase-intrinsic volume-averaged quantities are defined as,

$$\langle u \rangle^\gamma(\boldsymbol{x}, t) \equiv \frac{1}{V_\gamma(\boldsymbol{x})}\int_{\zeta\in\mathcal{V}_\gamma(\boldsymbol{x})} u(\zeta, t)\, dV_\zeta, \qquad [8]$$

where $V_\gamma(\boldsymbol{x}) \equiv \int_{\zeta\in\mathcal{V}_\gamma(\boldsymbol{x})} dV_\zeta$. Note that we use a simplified version of the averaging operator, and that the general definition employs a spatial convolution.[41–43] The phase-intrinsic average can describe either the electrolyte or the AM, $\gamma \in \{e, k\}$, and the phase volume fraction is defined as,

$$\varepsilon_\gamma \equiv \frac{V_\gamma(\boldsymbol{x})}{V}, \qquad [9]$$

where $V \equiv \int_{\zeta\in\mathcal{V}(\boldsymbol{x})} dV_\zeta$ is the volume of the entire averaging set. The surface-average operator is defined as,

$$\langle u\rangle_A(\boldsymbol{x},\, t) \equiv \frac{1}{A(\boldsymbol{x})}\int_{\zeta\in\mathcal{A}_\gamma(\boldsymbol{x})} u(\zeta,\, t)dA_\zeta, \qquad [10]$$

where $A(\boldsymbol{x}) \equiv \int_{\zeta\in\mathcal{A}_\gamma(\boldsymbol{x})} dA_\zeta$, and the internal boundary between electrolyte and AM in the averaging set is $\mathcal{A}(\boldsymbol{x}) \subset \partial\Omega_{k,e}$. We will assume that $V_\gamma(\boldsymbol{x})$ and $A(\boldsymbol{x})$ do not vary significantly with $\boldsymbol{x}$—in other words, the total phase volume and interface area within an averaging set do not change significantly when the centroid of the averaging set is moved. The following theorems, which are classical in the VAT,[7] are employed throughout this section (see Plett's work[12] for their derivation),

$$\begin{aligned}\langle\nabla\cdot\boldsymbol{u}\rangle^\gamma &= \nabla\cdot\langle\boldsymbol{u}\rangle^\gamma + \frac{1}{V_\gamma}\int_{\mathcal{A}(\boldsymbol{x})}(\boldsymbol{n}\cdot\boldsymbol{u})dA \quad \text{Theorem 1},\\ \langle\nabla u\rangle^\gamma &= \nabla\langle u\rangle^\gamma + \frac{1}{V_\gamma}\int_{\mathcal{A}(\boldsymbol{x})}(\boldsymbol{n}u)dA \quad \text{Theorem 2}.\end{aligned}$$

Note that a more general form of the above theorems can be found in the VAT literature,[8] and they have been simplified here with the assumption that $V_\gamma(\boldsymbol{x})$ does not vary significantly with $\boldsymbol{x}$ (which is commonly written as $\nabla\varepsilon_\gamma \approx 0$).

Averaging the AM mass balance.—We begin by decomposing the microscale AM domain Ω_k into subdomains for each AM particle, Ω_{k_i}, where i is the particle index—this is illustrated in Fig. 1. Writing Eqs. 1b and 1d in this form and inserting the flux expression (Eq. 3c) gives,

$$\partial_t c_{k_i} = \nabla\cdot(D_k\,\nabla c_{k_i}) \qquad \text{in } \Omega_{k_i}, \qquad [11a]$$

$$-\boldsymbol{n}\cdot D_k\,\nabla c_{k_i} = F^{-1}j_{k_i} \qquad \text{at } \partial\Omega_{k_i,e}. \qquad [11b]$$

Now, an extra BC is required to describe transport at the boundary between Particle i and Particle j (a neighbouring particle), $\partial\Omega_{k_i,k_j}$—we consider two options for this. Option 1 uses the exact BCs that exist between particles in the microscale model,

$$\boldsymbol{n}\cdot\boldsymbol{N}_{k_i} = \boldsymbol{n}\cdot\boldsymbol{N}_{k_j} \qquad \text{at } \partial\Omega_{k_i,k_j}, \qquad [12a]$$

$$c_{k_i} = c_{k_j} \qquad \text{at } \partial\Omega_{k_i,k_j}, \qquad [12b]$$

where $\boldsymbol{n}$ is the normal vector pointing outwards from Particle i in this context. In Option 2, we instead argue that in a real electrode, high transport resistance at grain boundaries largely prevents lithium diffusion between particles.[9,44,45] We therefore assume that

$$\boldsymbol{n}\cdot\boldsymbol{N}_{k_i} \approx 0 \qquad \text{at } \partial\Omega_{k_i,k_j}. \qquad [13]$$

The advantage of this approach is that it greatly simplifies the closure problems developed below, which can consequently be solved independently for Particles i and j. Continuing with the VAT, we homogenise Eq. 11a (unlike in the DFN) by applying the definition in Eq. 8,

$$\langle\partial_t c_{k_i}\rangle^k = \langle\nabla\cdot(D_k\,\nabla c_{k_i})\rangle^k. \qquad [14]$$

We assume that the boundaries within the averaging volume ($\partial\Omega_{k_i,e}$ and $\partial\Omega_{k_i,k_j}$) do not evolve temporally. Since the limits of the averaging volume integration are also independent of time, integration and differentiation can be exchanged in the first term, and thus $\langle\partial_t c_{k_i}\rangle^k = \partial_t\langle c_{k_i}\rangle^k$. Using Theorem 1 gives,

$$\begin{aligned}\partial_t\langle c_{k_i}\rangle^k = {}&\nabla\cdot\langle D_k\,\nabla c_{k_i}\rangle^k\\ &+\frac{1}{V_{k_i}}\int_{\mathcal{A}_i}(\boldsymbol{n}\cdot D_k\,\nabla c_{k_i})dA,\end{aligned} \qquad [15]$$

and the integral in the above equation can be substituted using Eq. 1d and subsequently written using the surface average notation (Eq. 10),

$$\partial_t\langle c_{k_i}\rangle^k = \nabla\cdot\langle D_k\,\nabla c_{k_i}\rangle^k - \frac{A_i}{FV_{k_i}}\langle j_{k_i}\rangle_A. \qquad [16]$$

Neglecting the variation of D_k over the scale of the averaging volume and applying Theorem 2,

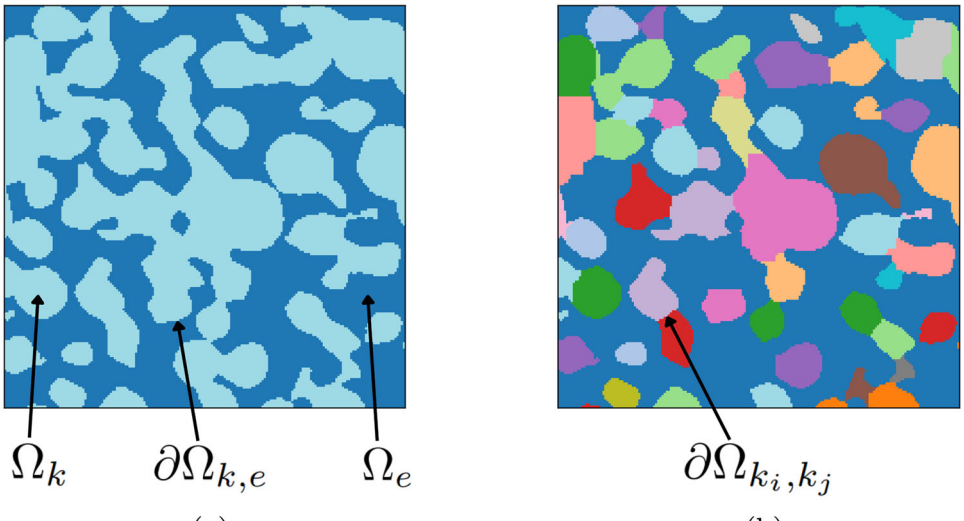

Figure 1. An illustration of the decomposition of Ω_k (a) into subdomains for each AM particle (b), Ω_{k_i}, where each particle is shown in a different colour.

$$\partial_t \langle c_{k_i} \rangle^k = \nabla \cdot \left[D_k \left(\nabla \langle c_{k_i} \rangle^k + \frac{1}{V_{k_i}} \int_{\mathcal{A}_i} \boldsymbol{n} c_{k_i} dA \right) \right] - \frac{A_i}{F V_{k_i}} \langle j_{k_i} \rangle_A. \quad [17]$$

The concentration in the above equation will be decomposed into an average and a deviation from the average, $c_{k_i} = \langle c_{k_i} \rangle^k + \tilde{c}_{k_i}$,

$$\partial_t \langle c_{k_i} \rangle^k = \nabla \cdot D_k \left(\nabla \langle c_{k_i} \rangle^k + \frac{1}{V_{k_i}} \int_{\mathcal{A}_i} \boldsymbol{n} \langle c_{k_i} \rangle^k dA + \frac{1}{V_{k_i}} \int_{\mathcal{A}_i} \boldsymbol{n} \tilde{c}_{k_i} dA \right) - \frac{A_i}{F V_{k_i}} \langle j_{k_i} \rangle_A. \quad [18]$$

One term will be neglected using the following logic, which is a standard approach in the VAT,[7]

$$\frac{1}{V_{k_i}} \int_{\mathcal{A}_i} \boldsymbol{n} \langle c_{k_i} \rangle^k |_{\boldsymbol{x}} \, dA = \langle c_{k_i} \rangle^k |_{\boldsymbol{x}} \frac{1}{\varepsilon_{k_i} V_i} \int_{\mathcal{A}_i} \boldsymbol{n} dA = -\langle c_{k_i} \rangle^k |_{\boldsymbol{x}} \frac{\nabla \varepsilon_{k_i}}{\varepsilon_{k_i}} \approx 0, \quad [19]$$

where $\varepsilon_{k_i} V_i = V_{k_i}$, giving,

$$\partial_t \langle c_{k_i} \rangle^k = \nabla \cdot D_k \left(\nabla \langle c_{k_i} \rangle^k + \frac{1}{V_{k_i}} \int_{\mathcal{A}_i} \boldsymbol{n} \tilde{c}_{k_i} dA \right) - \frac{A_i}{F V_{k_i}} \langle j_{k_i} \rangle_A. \quad [20]$$

Finally, we use the following order of magnitude comparison,

$$\nabla \cdot D_k \left(\nabla \langle c_{k_i} \rangle^k + \frac{1}{V_{k_i}} \int_{\mathcal{A}_i} \boldsymbol{n} \tilde{c}_{k_i} dA \right) \ll \frac{A_i}{F V_{k_i}} \langle j_{k_i} \rangle_A. \quad [21]$$

This says that the *macroscale* diffusion flux within the AM is negligible compared to the reaction source term. Although the DC model could easily be developed without this assumption (a demonstration is given in the SM), this reflects the argument (introduced above) that high transport resistance largely prevents lithium diffusion across inter-particle boundaries.[9,44,45] Inserting this assumption gives

$$\partial_t \langle c_{k_i} \rangle^k = -\frac{A_i}{F V_{k_i}} \langle j_{k_i} \rangle_A. \quad [22]$$

We now have a homogenised equation for $\langle c_{k_i} \rangle^k$, which is a function of the macroscale source term $\langle j_{k_i} \rangle_A$. Nonetheless, the micro and macroscale problems are still coupled at this point, as j_{k_i} depends on all microscale variables.

The closure problem.—To decouple the micro and macroscale problems (obtain "closure"), we seek to approximate j_{k_i} as a function of macroscale variables. To estimate a macroscale surface concentration, $\langle c_{k_i} \rangle_A$, we will define a mapping between $\langle c_{k_i} \rangle^k$ and $\langle c_{k_i} \rangle_A$ using a closure problem. As per the VAT, the process begins by finding a PDE on $\tilde{c}_{k_i}$, in order to identify source terms causing deviations in concentration across the averaging volume. To do so, we first insert the assumption used above, $D_k \nabla \langle c_{k_i} \rangle^k \approx 0$ into Eq. 11a, and then Eq. 22 is subtracted from the result,

$$\partial_t \tilde{c}_{k_i} = \nabla \cdot (D_k \nabla \tilde{c}_{k_i}) + \frac{A_i}{F V_{k_i}} \langle j_{k_i} \rangle_A. \quad [23]$$

An important assumption is made at this point—that the closure problem is quasi-steady,[6] and thus $\partial_t \tilde{c}_{k_i} \approx 0$. We revisit this assumption in Part II of this work. Equation 23 may subsequently be written as,

$$\Delta \tilde{c}_{k_i} = -\frac{1}{F D_k} \frac{A_i}{V_{k_i}} \langle j_{k_i} \rangle_A. \quad [24]$$

The BC at $\partial \Omega_{k,e}$ is now considered, with the assumption that $D_k \nabla \langle c_{k_i} \rangle^k \approx 0$ as in the PDE (discussed in the SM). However, an additional approximation is required to describe $\tilde{c}_{k_i}$ as a function of macroscale source terms exclusively, as Eq. 11b still contains j_{k_i}. We therefore employ the hypothesis that the reaction rate does not vary significantly over the surface of any given particle, $j_{k_i} \approx \langle j_{k_i} \rangle_A$,

$$-\boldsymbol{n} \cdot D_k \nabla \tilde{c}_{k_i} = \frac{\langle j_{k_i} \rangle_A}{F} \quad \text{at } \partial \Omega_{k,e}. \quad [25]$$

Depending on the option used for inter-particle flux (discussed above), two different closure problems are reached.

Inter-particle flux option 1.—For Option 1, the BC at $\partial \Omega_{k_i,k_j}$ (Eq. 12) becomes

$$\boldsymbol{n} \cdot D_k \nabla c_{k_i} = \boldsymbol{n} \cdot D_k \nabla c_{k_j} \quad \text{at } \partial \Omega_{k_i,k_j}, \quad [26a]$$

$$c_{k_i} = c_{k_j} \quad \text{at } \partial \Omega_{k_i,k_j}. \quad [26b]$$

We use the argument of high transport resistance at grain boundaries (introduced above) to justify the following assumptions,

$$\nabla \langle c_{k_\alpha} \rangle^k \ll \nabla \tilde{c}_{k_\alpha}, \quad [27a]$$

$$\langle c_{k_i} \rangle^k \approx \langle c_{k_j} \rangle^k, \quad [27b]$$

where $\alpha \in \{i, j\}$. Employing these assumptions in the BCs gives,

$$\boldsymbol{n} \cdot D_k \nabla \tilde{c}_{k_i} = \boldsymbol{n} \cdot D_k \nabla \tilde{c}_{k_j} \quad \text{at } \partial \Omega_{k_i,k_j}, \quad [28a]$$

$$\tilde{c}_{k_i} = \tilde{c}_{k_j} \quad \text{at } \partial \Omega_{k_i,k_j}. \quad [28b]$$

This couples the closure problems for different particles, and leads us to suggest the following closure,

$$\tilde{c}_{k_i} = s_{ii} \langle j_{k_i} \rangle_A + s_{ij} \langle j_{k_j} \rangle_A, \quad [29a]$$

$$\tilde{c}_{k_j} = s_{ji} \langle j_{k_i} \rangle_A + s_{jj} \langle j_{k_j} \rangle_A, \quad [29b]$$

where s_{ii}, s_{ij}, s_{ji}, and s_{jj} are mapping/closure variables. Finally, we argue that the average reaction rates for two neighbouring particles are relatively similar, and thus $\langle j_{k_i} \rangle_A \approx \langle j_{k_j} \rangle_A$, giving

$$\tilde{c}_{k_i} = s_i \langle j_{k_i} \rangle_A, \quad [30a]$$

$$\tilde{c}_{k_j} = s_j \langle j_{k_j} \rangle_A, \quad [30b]$$

where $s_i = s_{ii} + s_{ij}$ and $s_j = s_{ji} + s_{jj}$. This reduces the strength of the coupling between the closure for Particles i and j, and the final problem for s_i is

$$\Delta s_i = -\frac{1}{FD_k}\frac{A_i}{V_{k_i}} \qquad \text{in } \Omega_{k_i}, \tag{31a}$$

$$\boldsymbol{n}\cdot\nabla s_i = -\frac{1}{FD_k} \qquad \text{at } \partial\Omega_{k_i,e}, \tag{31b}$$

$$\boldsymbol{n}\cdot\nabla s_i = \boldsymbol{n}\cdot\nabla s_j \qquad \text{at } \partial\Omega_{k_i,k_j}, \tag{31c}$$

$$s_i = s_j \qquad \text{at } \partial\Omega_{k_i,k_j}. \tag{31d}$$

Note that the closure can also be cast in dimensionless form (provided in the SM), which removes the dependency on D_k and thus the problem solely depends on electrode geometry. For more discussion on the coupling of closure problems for s_i and s_j, see Davit's work.[46]

Inter-particle flux option 2.—For Option 2, the BC at $\partial\Omega_{k_i,k_j}$ (Eq. 13) becomes

$$\boldsymbol{n}\cdot\nabla\tilde{c}_{k_i} = 0 \qquad \text{at } \partial\Omega_{k_i,k_j}, \tag{32}$$

after the introduction of $D_k\,\nabla\langle c_{k_i}\rangle^k \approx 0$. From inspection of the PDE and BCs on $\tilde{c}_{k_i}$ (Eqs. 23, 25 and 32), it is evident that the only macroscale source term causing deviations in c_{k_i} from its average value is $\langle j_{k_i}\rangle_A$. We therefore propose the following closure,

$$\tilde{c}_{k_i} = s_i\langle j_{k_i}\rangle_A. \tag{33}$$

When inserted in Eqs. 23, 25, and 32 this gives the following closure problem,

$$\Delta s_i = -\frac{1}{FD_k}\frac{A_i}{V_{k_i}} \qquad \text{in } \Omega_{k_i}, \tag{34a}$$

$$\boldsymbol{n}\cdot\nabla s_i = -\frac{1}{FD_k} \qquad \text{at } \partial\Omega_{k_i,e}, \tag{34b}$$

$$\boldsymbol{n}\cdot\nabla s_i = 0 \qquad \text{at } \partial\Omega_{k_i,k_j}. \tag{34c}$$

Macroscale.—We seek to develop a macroscale equation on $\langle c_k\rangle^k$ rather than $\langle c_{k_i}\rangle^k$. To do so we make the assumption that the AM particles within each averaging volume can be represented by the population of AM particles across the entire electrode. Returning to Eq. 22 (describing $\langle c_{k_i}\rangle^k$), this can be written as,

$$\frac{V_{k_i}}{V_k}\partial_t\langle c_{k_i}\rangle^k = -\frac{A_i}{FV_k}\langle j_{k_i}\rangle_A. \tag{35}$$

By summing across the population of particles we obtain

$$\partial_t\langle c_k\rangle^k = -\frac{1}{FV_k}\sum_{i=1}^{n} A_i\langle j_{k_i}\rangle_A, \tag{36}$$

since $\partial_t\langle c_k\rangle^k \equiv \sum_{i=1}^{n}\frac{V_{k_i}}{V_k}\partial_t\langle c_{k_i}\rangle^k$, where n is the number of particles in Ω. Finally, we recognise that $\sum_{i=1}^{n} A_i\langle j_{k_i}\rangle_A = A\langle j_k\rangle_A$, thus giving

$$\partial_t\langle c_k\rangle^k = -\frac{A}{FV_k}\langle j_k\rangle_A. \tag{37}$$

As above, j_k still depends on all microscale variables, ϕ_e, c_e, ϕ_k, and c_k. For the former three variables, we will employ the same assumption that is used in the DFN[9] and both DC models found in the literature,[28,32]

$$c_e \approx \langle c_e\rangle^e, \tag{38a}$$

$$\phi_e \approx \langle\phi_e\rangle^e, \tag{38b}$$

$$\phi_k \approx \langle\phi_k\rangle^k. \tag{38c}$$

The treatment of c_k is the defining factor that separates the models. Two options are considered below.

Zeroth-order macroscale model (DC^0).—A crude approximation of $\langle c_k\rangle_A$, which will herein be referred to as the zeroth-order model, DC^0, could be made by assuming,

$$\langle c_k\rangle_A^0 = \langle c_k\rangle^k. \tag{39}$$

This produces the model used by Arunachalam and Onori,[32] which does not provide a correction between $\langle c_k\rangle^k$ and $\langle c_k\rangle_A$. Here, this is referred to as a zeroth-order DC model, DC^0,

$$\partial_t\langle c_k\rangle^k = -\frac{A}{FV_k}j_k^0, \tag{40}$$

where $j_k^0(\langle c_e\rangle^e, \langle\phi_e\rangle^e, \langle\phi_k\rangle^k, \langle c_k\rangle_A^0)$ is defined precisely in Eq. 53.

First-order macroscale model (DC^1).—With knowledge of the mapping variable developed above, the zeroth-order model can be improved. To illustrate an assumption, the definition of c_{k_i} will be written as

$$c_{k_i} = \langle c_k\rangle^k + (\langle c_{k_i}\rangle^k - \langle c_k\rangle^k) + s_i\langle j_{k_i}\rangle_A. \tag{41}$$

We argue that $(\langle c_{k_i}\rangle^k - \langle c_k\rangle^k) \ll s_i\langle j_{k_i}\rangle_A$. This is in line with the undergirding philosophy of the model—that the surface reaction drives microscale deviations in c_k, and is much more dominant than flux between particles. Thus,

$$c_{k_i} \approx \langle c_k\rangle^k + s_i\langle j_{k_i}\rangle_A. \tag{42}$$

The surface average over all particles within the averaging volume can be written as,

$$\langle c_k\rangle_A \equiv \frac{1}{A}\sum_{i=1}^{n}\int_{\mathcal{A}_i} c_{k_i}\,dA. \tag{43}$$

We build a first-order approximation of surface concentration, $\langle c_k\rangle_A^1$, by substituting Eq. 42 into Eq. 43, and employing the assumption that $\langle j_{k_i}\rangle_A$ does not vary significantly across the population of particles within an averaging volume, $\langle j_{k_i}\rangle_A \approx \langle j_k\rangle_A$,

$$\langle c_k\rangle_A^1 = \langle c_k\rangle^k + \langle j_k\rangle_A\langle s\rangle_A, \tag{44}$$

where,

$$\langle s\rangle_A = \frac{1}{A}\sum_{i=1}^{n}\int_{\mathcal{A}_i} s_i\,dA. \tag{45}$$

This improved estimate of the surface concentration can be used in the reaction rate expression giving the final PDE,

$$\partial_t\langle c_k\rangle^k = -\frac{A}{FV_k}j_k^1, \tag{46}$$

where $j_k^1(\langle c_e\rangle^e, \langle\phi_e\rangle^e, \langle\phi_k\rangle^k, \langle c_k\rangle_A^1)$ is defined precisely in Eq. 53. Finally, since we do not know $\langle j_k\rangle_A$ *a priori,* we assume that $\langle j_k\rangle_A \approx j_k^1$ (an alternative approach is given in the SM),

$$\langle c_k\rangle_A^1 = \langle c_k\rangle^k + \langle s\rangle_A j_k^1. \quad [47]$$

This model is the centerpiece of this work, and will be referred to as the first-order DC model, DC[1]. We highlight that Eq. 46 is *not* an ordinary differential equation, since j_k^1 is a function of spatial position.

Yang's model (DC^y).—Yang and Tartakovsky's DC model[28] (introduced above and herein referred to as DC^y) used boundary-layer theory to approximate the surface concentration, in which the thickness of the boundary layer is given by,

$$l_d = \begin{cases} a_d\sqrt{D_k t}, & 0 < t < t_d/a_d^2, \\ l_k, & \text{otherwise}, \end{cases} \quad [48]$$

where l_k is the characteristic particle length, a_d is a dimensionless fitting parameter, and $t_d = \frac{l_k^2}{D_k}$. Within the boundary layer, they use a second-order polynomial to describe c_k, and assume that it is uniform outside this layer. The resulting relationship for surface concentration, $\langle c_k\rangle_A^y$, is

$$\langle c_k\rangle_A^y = \langle c_k\rangle^k + \gamma j_k^y, \quad [49]$$

where

$$\gamma = \left(\frac{l_d^2}{6l_k^2} - \frac{l_d}{2l_k}\right)\frac{l_k}{D_k F}, \quad [50]$$

and the precise definition of $j_k^y(\langle c_e\rangle^e, \langle\phi_e\rangle^e, \langle\phi_k\rangle^k, \langle c_k\rangle_A^y)$ is given in Eq. 53.

The DFN.—Since the AM mass balance is not homogenised in the DFN (as in the DC models), we have $c_k(\boldsymbol{x}, r, t)$ rather than $\langle c_k\rangle^k(\boldsymbol{x}, t)$. The AM mass balance solved on the radial (microscale) dimension is given by,

$$\partial_t c_k = -\frac{1}{r^2}\frac{\partial}{\partial r}(r^2 N_k) \qquad \text{for } 0 \leqslant r \leqslant R_k, \quad [51a]$$

$$N_k = \frac{j_k^d}{F} \qquad \text{at } r = R_k, \quad [51b]$$

$$N_k = 0 \qquad \text{at } r = 0, \quad [51c]$$

where,

$$N_k = -D_k\frac{\partial c_k}{\partial r}. \quad [52]$$

The DFN in its standard form implicitly requires the assumption that c_k does not vary over a particle surface. Nonetheless for consistency of notation, we will define a surface average $\langle c_k\rangle_A^d = c_k|_{R_k}$. The precise definition of $j_k^d(\langle c_e\rangle^e, \langle\phi_e\rangle^e, \langle\phi_k\rangle^k, \langle c_k\rangle_A^d)$ is given in Eq. 53.

Model differences.—The way in which j_k is calculated gives rise to key differences between each model. To be explicit, four approximations are defined, all using the BV equation and differing only in their estimate of surface concentration, $\langle c_k\rangle_A$,

Table I. The surface concentration definitions for each model.

Model	Surface concentration
DC^0	$\langle c_k\rangle_A^0 = \langle c_k\rangle^k$
DC^1	$\langle c_k\rangle_A^1 = \langle c_k\rangle^k + \langle s\rangle_A j_k^1$
DC^y	$\langle c_k\rangle_A^y = \langle c_k\rangle^k + \left(\frac{l_d^2}{6l_k^2} - \frac{l_d}{2l_k}\right)\frac{l_k}{D_k F} j_k^y$
DFN	$\langle c_k\rangle_A^d = c_k\|_{R_k}$

$$j_k^m = 2j_{k0}^m \sinh\left(\frac{F}{2RT}\eta_k^m\right), \quad [53]$$

where $m \in \{0, 1, \mathrm{d}, y\}$ and

$$\eta_k^m = \langle\phi_k\rangle^k - \langle\phi_e\rangle^e - U_k(\langle c_k\rangle_A^m), \quad [54a]$$

$$j_{k0}^m = Fk_k\sqrt{\langle c_k\rangle_A^m\langle c_e\rangle^e(c_{k,\max} - \langle c_k\rangle_A^m)}. \quad [54b]$$

The surface concentration definitions are summarised in Table I—note that in all models, the functions j_k^m and $\langle c_k\rangle_A^m$ are coupled. The remaining equations for all models are identical, and thus are provided in the SM.

Validation Using DNS

Methodology.—To validate the first-order DC model developed above (DC[1]), we compare its cell-voltage prediction to that of the DNS, DFN, DC[0], and DC^y. In all cases explored, the AM is made of nickel manganese cobalt oxides (NMC). We first compare four 2D electrodes: overlapping particles with a uniform radius of 4.95 μm (A), fractured particles (B), a distribution of particle radii (C), and an artificial electrode slice (D). The motivation for this choice will become clear in the discussion section. The resulting half-cells and the solutions to the closure problem for each electrode are shown in Fig. 2. Following this, the models were compared for a 3D electrode constructed from a tomographic image—a crop of 190 × 190 × 190 voxels was taken from the center of the "Cal-2" data set published by Usseglio-Viretta et al.[47] (see Fig. 4 for the structure and closure solution). Our primary simulation protocol is a 1C discharge to 3.0 V, followed by a 15-minute relaxation period (see the SM for C-rate calculation details). All models are solved across all electrodes for this baseline case. To illustrate key model behaviours, we also consider two additional scenarios. In both of these, the upper voltage limit is increased to 3.5 V. In the second, the AM diffusivity is reduced by a factor of five. We arbitrarily chose Electrode B to demonstrate these additional cases.

One of the purposes of the 2D electrodes is to facilitate comprehension of the mapping variable, since it is straightforward to visualise. In all cases, Option 1 was used to solve the closure problem, although the values of $\langle s\rangle_A$ obtained using Option 2 were not strikingly different (see the SM for comparison). The primary appeal of Option 2 is that it decouples the closure problems for different particles, significantly reducing computation time.

Electrode B was built by manually adding fractures to Electrode A—note that for Electrode B, the length scale parameter used in the DFN and DC^y models is smaller than that for Electrode A (1.83 μm vs 4.95 μm), since the fractures significantly reduce the mean length scale over which diffusion occurs. For Electrode C, 30 radii were randomly sampled from a normal distribution with a mean of 3.75 μm and a standard deviation of 2.25 μm (which is a plausible distribution for NMC particles[35]). For D, a field of random noise was generated, to which Gaussian smoothing was then applied, followed by a global threshold to separate particles from the background—this mimics the "blobby" like structure of real NMC electrodes.

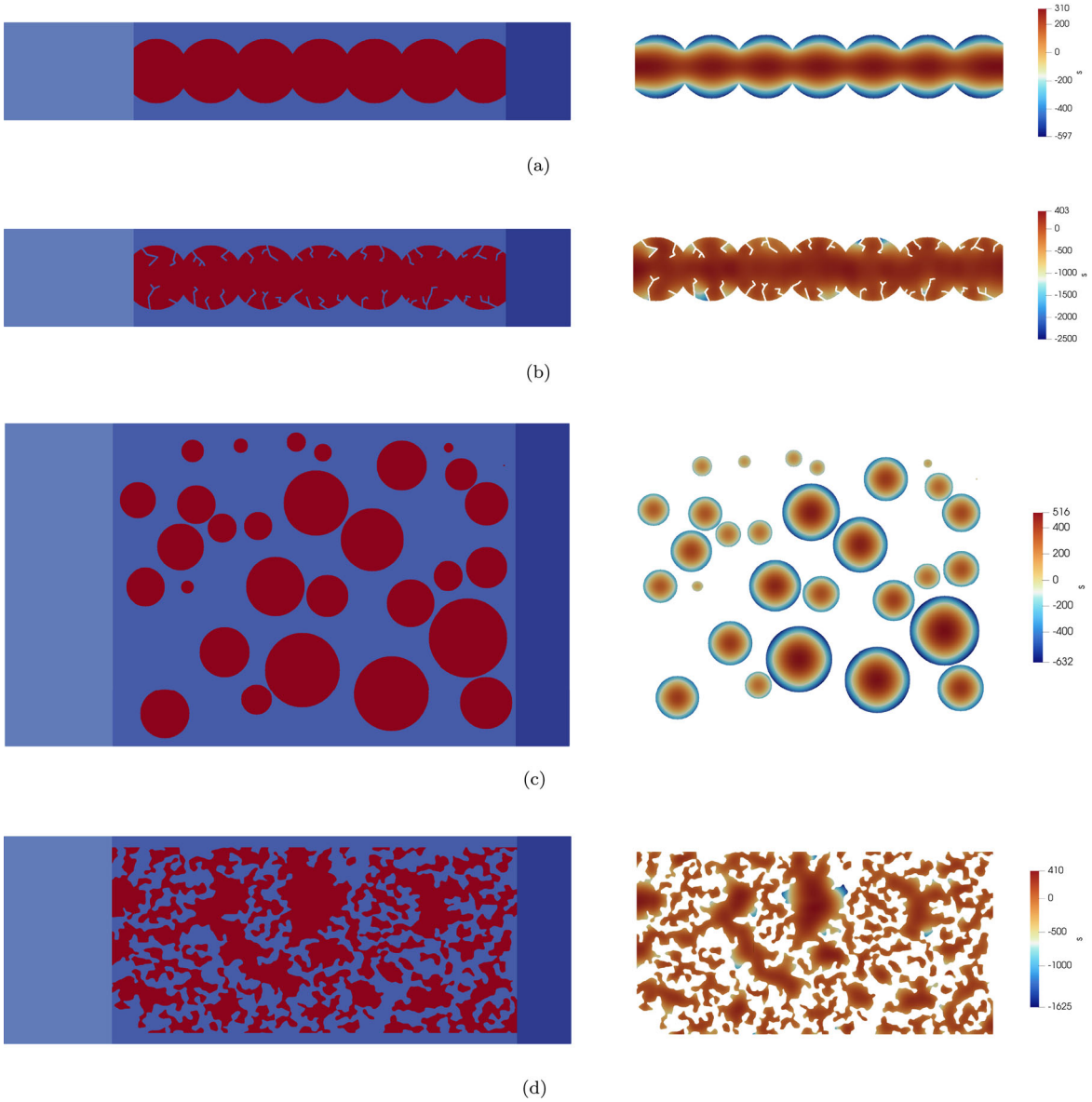

Figure 2. The half-cells (left) and corresponding solutions for s with units of mol·m^{-1}A^{-1} (right). Electrodes A, B, C, and D are shown from top to bottom. The effective separator is on the left of each half cell, whilst electrolyte is shown in blue, AM in red, and the current collector in dark blue. The lithium foil is not shown here, but is on the leftmost boundary of the separator.

All DNS results were obtained using an in-house code which solves the microscale model exactly as outlined in Eqs. 1 through 5 using a finite-volume scheme and a voxel-based mesh, and has been validated against BEST[48,49] and COMSOL Multiphysics.[50] The DFN and all DC models were solved using PyBaMM.[51] The material properties and effective properties are given in Tables II and III respectively, and further solver details are given in the SM.

An initial AM concentration of 25,000 mol·m^{-3} was used, corresponding to a lithium stoichiometry of ∼0.5. This is slightly higher than values used in other articles (e.g. 0.37[28,36]). Effectively, this corresponds to discharging a battery which is initially at a lower state of charge. We do not expect this to influence the conclusions drawn from our results, since the principal differences between models are seen toward the end of the discharge and during the relaxation.

Effective transport properties were calculated directly from the microstructure, by solving Laplace's equation using Taufactor.[54] Additionally, the calculations were validated using the in-house code introduced above, following the method outlined by Kehrwald et al.[55] The surface area for reaction, A was also calculated directly from the electrode images, summing the area of voxel faces at $\partial\Omega_{k,e}$. To solve the closure problem, and also to define a particle radius for the DFN and DC^y, particle boundaries must be defined—a watershed approach was used to do so (see the SM). The length scales of all particles were averaged using an arithmetic mean to set R_k and l_k for the DFN and DC^y respectively,

$$R_k = l_k = \frac{1}{n}\sum_{i=1}^{n} l_i, \qquad [55]$$

where l_i is the length scale of Particle i. Finally, the closure problems (Eqs. 31 or 34) were solved using OpenFOAM's chtMultiRegionFoam solver. A Python model, "solveclosure", was developed to automate the solution of the problem, allowing the user to obtain results for s_i by simply providing an electrode image. This has been made publicly available,[56] to make DC[1] accessible and our results reproducible. Whilst articles using the VAT often solve the closure problem on a "representative" subsection, we choose to solve it for the entire electrode domains, to capture the statistical properties of the geometries

Table II. The material properties and initial conditions used.

Property Name	Symbol	Value	Ref.
Thermodynamic factor	$(1 + \delta_e)$	1	52
Transference number	t_+^0	0.4	52
Electrolyte conductivity [S·m^{-1}]	σ_e	1	52
Electrolyte diffusivity [m^{2}s^{-1}]	D_e	1×10^{-10}	52
Initial electrolyte concentration [mol·m^{-3}]	$c_{e,0}$	1000	36
Initial AM concentration [mol·m^{-3}]	$c_{k,0}$	25000	n/a
Temperature [K]	T	298.15	n/a
Maximum AM concentration [mol·m^{-3}]	$c_{k,\max}$	50400	34
AM conductivity	σ_k	2.8	34
AM diffusivity [m^{2}s^{-1}]	D_k	4×10^{-14}	34
Separator tortuosity	$\tau_{e,s}$	2.28	53
Separator porosity	$\varepsilon_{e,s}$	0.4	53
Separator surface porosity	$\varepsilon_{e,s}^{\text{surf}}$	1	n/a
Positive electrode rate constant [Am^{-2}(m^{3}mol^{-1})$^{1.5}$]	Fk_k	4.824×10^{-6}	33, 35
Exchange-current density for lithium foil [Am^{-2}]	$j_{li,0}$	10	11

as accurately as possible. Indeed, a study could be performed on the correlation length of each geometry[57–59] to define a representative sub-volume, thus reducing the computational cost of the closure problem.

Discussion of DC^1.—The cell-voltage profiles for all models on all 2D electrodes are shown in Fig. 3, whilst the results for the 3D electrode are in Fig. 5. The correction offered by DC^1 is able to considerably improve the voltage prediction compared to DC^0, particularly towards the end of the discharge and during the relaxation. DC^1 also offers a superior voltage prediction compared to the DFN for all electrodes. The accuracy of DC^1 is greater than that of DC^y for all electrodes except Electrode A, where DC^y has a slight advantage—nonetheless, both DC^1 and DC^y are very precise for this case.

The improved voltage prediction offered by DC^1 is essentially a result of its enhanced estimate of AM surface concentration compared to the DFN—an example of this is illustrated in Fig. 5b. Since the cell voltage can be decomposed into the equilibrium potential plus a sum of overpotential contributions (see Schmidt's work[38] for an example), improving the estimate of $\langle c_k \rangle_A$ affects the cell-voltage output by refining the diffusion overpotential prediction. We argue that this improved estimate of surface concentration primarily results from eliminating the assumption that particles are isolated spheres, and instead incorporating the transport characteristics of the real microstructure via the closure problem.

Towards the end of the discharge in Figs. 3 and 5a, the AM is highly lithiated and thus a steep region of the OCP curve is encountered (see Fig. 10 in the SM). Therefore, a small change in stoichiometry causes a large change in voltage, explaining the significant differences in cell voltage observed during the relaxation period (stoichiometry at the end of discharge is provided in the SM, Tables 6 and 7). To demonstrate a scenario where this steep region of the OCP curve has less influence, a case was solved in which the discharge was terminated at 3.5 V (Fig. 6a). Differences still exist between the relaxation voltages for each model, albeit less pronounced. However, this simulation highlights the subtle differences between the cell-voltage for each model throughout the *discharge*, which were less clear in Figs. 3 and 5a.

Since DC^1's improved cell-voltage prediction results from its approach to modelling diffusion in the AM microstructure, we expect its advantage to be accentuated for cases where diffusion is more limiting. To confirm this, we reduced the AM diffusivity by a factor of five—results are shown in Fig. 6b. Here, we indeed observe larger differences between the discharge termination time (and thus final lithiation) for each model. Likewise, the difference between voltage for DC^1 and DC^y throughout the discharge is also highlighted. Although DC^1's accuracy is lower at the start of the discharge for this case, this phenomenon is studied in Part II, and we present an extension which resolves the problem very well.

One potential criticism of our methods is the use of constant material properties for the AM and electrolyte, since these can depend strongly on c_k and c_e respectively. We consider constant values a good starting point, as they demonstrate the performance of the models whilst minimising complexity, and numerous articles in the literature employ this approach for the electrolyte and/or the AM.[28,34–36,60,61] Nonetheless, to confirm that the use of non-constant material properties does not alter our conclusions, an extra case is included in the SM, in which D_e, σ_e, and the thermodynamic factor $(1 + \delta_e)$ are functions of c_e, and D_k is a function of c_k. These results support the claim that our conclusions (most importantly regarding the performance of DC^1) will still be valid when material properties are non-linear functions of state variables.

The primary challenge faced when using DC^1 is the solution of the closure problem, which can be a relatively large computation. However, we highlight that the user need only perform this calculation *once* per electrode—the closure problem is independent of discharge rate, material properties, operating conditions, etc. Furthermore, if desired, one can simply treat $\langle s \rangle_A$ as a fitting parameter, avoiding the solution of a closure problem (discussed in more detail below). The time required to solve the closure problem for each electrode is provided in the SM (Table 9). For the 2D electrodes, this is generally in the order of one minute, with the exception of Electrode D since it contains more particle boundaries. For the 3D case, ∼12 hours are required. Nonetheless, this computation time could likely be reduced significantly by optimising the OpenFOAM parallelisation, workflow and solver choices—this has not been pursued yet.

Table III. Geometry information and effective properties for each electrode.

Parameter	A	B	C	D	3D
Length [μm]	57.3	57.3	75	75	75.62
Height [μm]	15	15	60	42.9	75.62
Depth [μm]	—	—	—	—	75.62
Particle radius [μm]	4.95	1.826	3.75	0.971	3.405
AM volume fraction	0.572	0.543	0.360	0.483	0.493
Effective conductivity, σ_p^{eff} [Sm^{-1}]	1.415	0.964	166.8	60.0	0.420
Electrolyte transport efficiency, $\mathfrak{B}_{e,p}$	0.394	0.394	0.445	0.160	0.291
Specific surface area, a_p [m^{-1}]	206806	488132	200533	736526	391290
$\langle s \rangle_A$ [mol·m^{-1}A^{-1}]	−492.3	−451.4	−388.0	−190.7	−416.7
γ [mol·m^{-1}A^{-1}]	−427.5	−157.7	−323.9	−83.9	−294.1

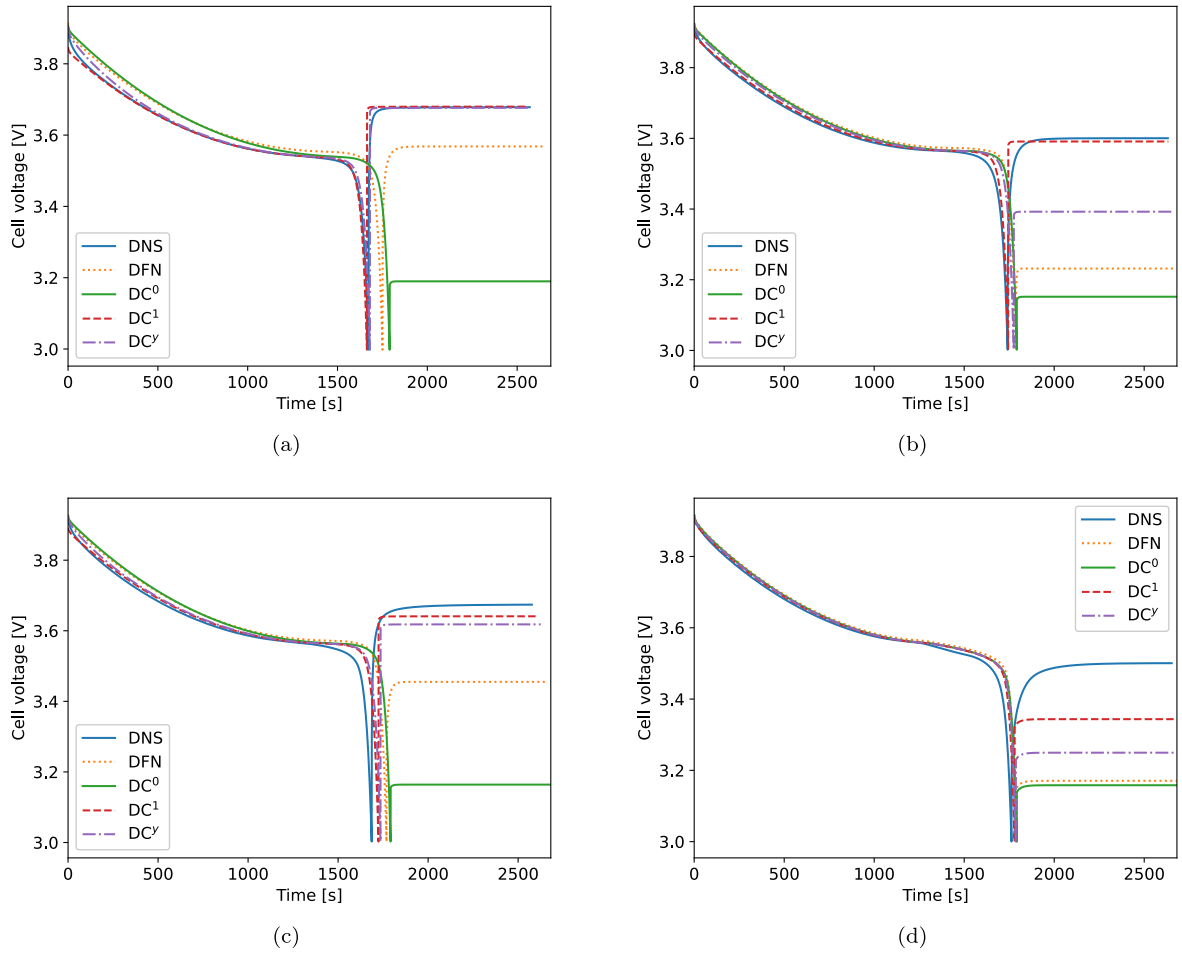

Figure 3. Cell-voltage profiles for 1C discharge-relaxation simulations on Electrodes A, B, C, and D.

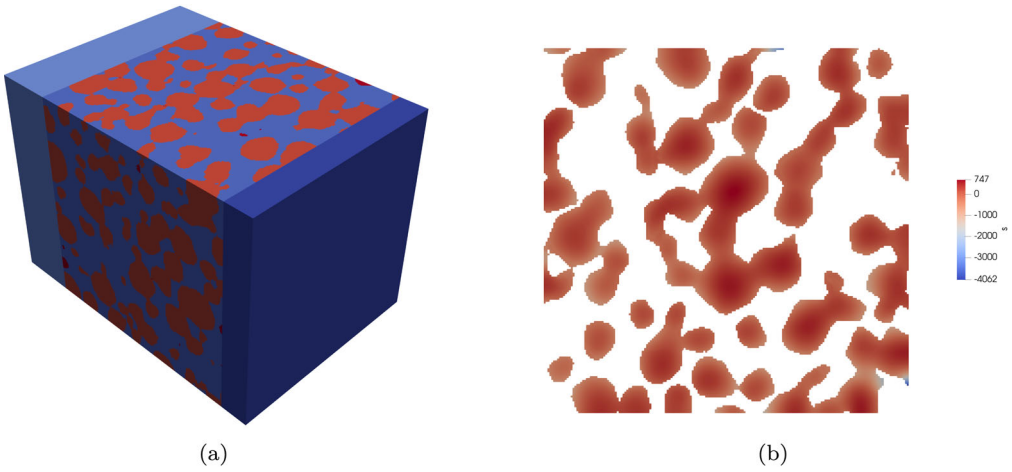

Figure 4. The 3D electrode (a) and the solution to the closure field over a slice arbitrarily taken from the centre of the electrode (b).

Discussion of DC^y.—As with DC^1, the correction for surface concentration offered by DC^y gives significant improvements compared to the model with no correction, DC^0. Similarly, DC^y consistently predicted cell-voltage better than the DFN. As for DC^1, we argue that DC^y is able to improve on the DFN by avoiding the assumption of isolated spherical particles.

The key challenge with DC^y is that it assumes the existence of a boundary layer, and thus relies on a particle length-scale parameter —the electrodes in this work have been chosen so as to highlight this complication. For Electrode A, DC^y performs very well, as a clear particle length scale exists. For Electrode B on the other hand, the performance of DC^y drops significantly, as there are now several length scales at play, due to the introduction of fractures. Likewise for Electrodes C, D and also the 3D case, we no longer have a clear definition of particle length scale. This challenge is not relevant for DC^1, as it does not assume the existence of a boundary layer.

The equation for surface concentration in DC^y takes a similar form to DC^1, in that a correction is calculated by multiplying the

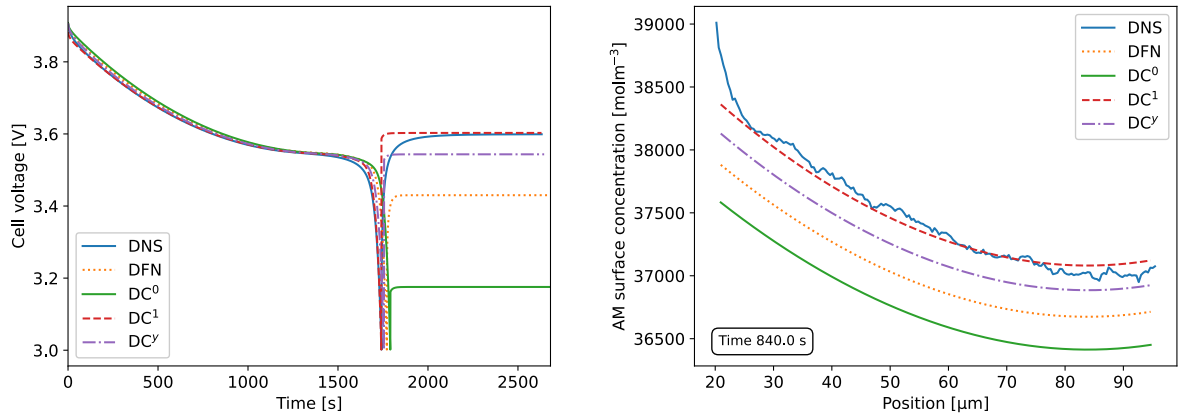

(a) (b)

Figure 5. Cell-voltage results for all models on the 3D half cell (a) and AM surface concentration (b) at an arbitrary time (840 s) into the discharge (the DNS results were averaged across each YZ plane along the electrode depth to obtain a 1D profile).

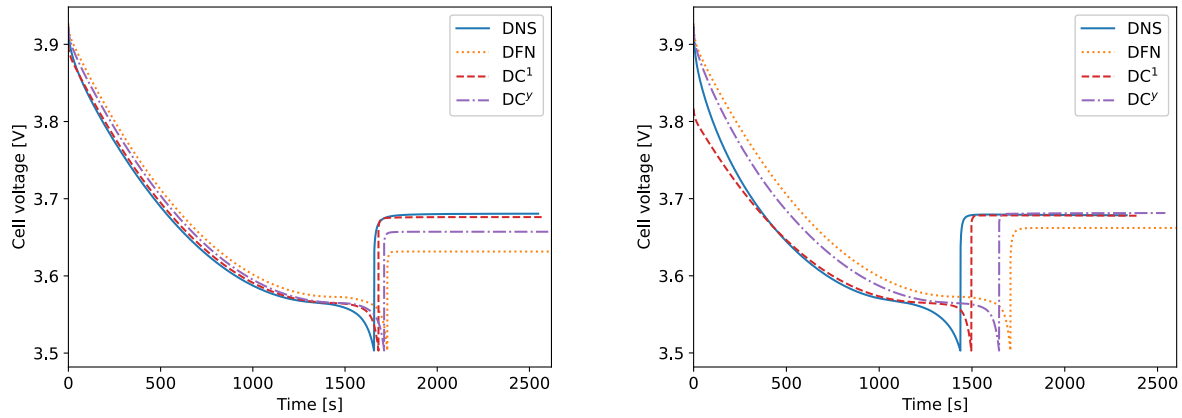

(a) (b)

Figure 6. Cell-voltage profiles for 1C discharge terminated at 3.5 V followed by a relaxation of 15 minutes on Electrode B, with $D_k = 4 \times 10^{-14}$ m^2s^{-1} (a) and $D_k = 8 \times 10^{-15}$ m^2s^{-1} (b).

reaction rate by a parameter—γ in the former (Eq. 50) and $\langle s \rangle_A$ in the latter. The magnitude of these parameters for each electrode is shown in Table III. Indeed, it would be possible to "tune" the length-scale parameter (and in turn the value of γ) so that DC^y matches the performance of DC^1. However, we would no longer be comparing the *predictive* ability of the models. Rather, our goal is to evaluate the accuracy of the models without relying on any form of optimisation, and keeping their parameterisation as similar as possible.

A second challenge concerning DC^y is the parameter a_d, which is described as a "fitting" parameter in the original work—this appears to introduce a semi-empirical nature to the model. Nonetheless, DC^y is clearly a reliable yet intuitive model. The simulations in this work serve as a further validation of DC^y, since in the original publication only a single microstructure was simulated.

Discussion of the DFN model.—The DFN's primary limitation is its assumption on particle shape, which is made to ease computational cost—it assumes the AM particles can be represented by isolated spheres, which may be far from reality. Furthermore, in the standard formulation of the DFN,[9] only a single sphere radius exists. Even for Electrode A, which contains a single radius, significant errors are seen in the DFN results largely due to two factors: the particles are not spherical but circular, and the particles are not isolated but overlap. For all other electrodes, the error becomes more pronounced, since the DFN's single particle radius is not able to capture the range of length scales present. Although modifications to the DFN exist which may improve performance, such as using a different specific surface area (a_k) value rather than the typical value of $\frac{3\epsilon_k}{R_k}$,[38] using cylindrical rather than spherical particles, or defining multiple particle sizes,[60] we have not considered these here for two reasons. Firstly, they are relatively rare in the literature, and thus we prefer to benchmark against a "standard" DFN model. Secondly, this work is not intended to be a review of the various possible formulations of the DFN.

A second important challenge which the DFN faces is similar to that of DC^y—it requires a radius parameter. For electrodes that are not composed of perfect circles/spheres, which is of course the case in a real battery, the definition of a particle radius becomes ambiguous. Contrastingly, DC^1 makes no assumption on the geometry of the microstructure, and solves a transport problem as close as possible to the initial microscale model. Similarly to our discussion above on the modifications of the DFN, various methods could be used to define a radius parameter for the model, but it is beyond the scope of this work to compare these—the reader is referred to Goldin's[39] work for such an analysis.

As for DC^y, the DFN's parameter set could also be "tuned" to better match the DNS data, but we would no longer be studying its *predictive* ability. With this in mind, we keep the parameterisation of

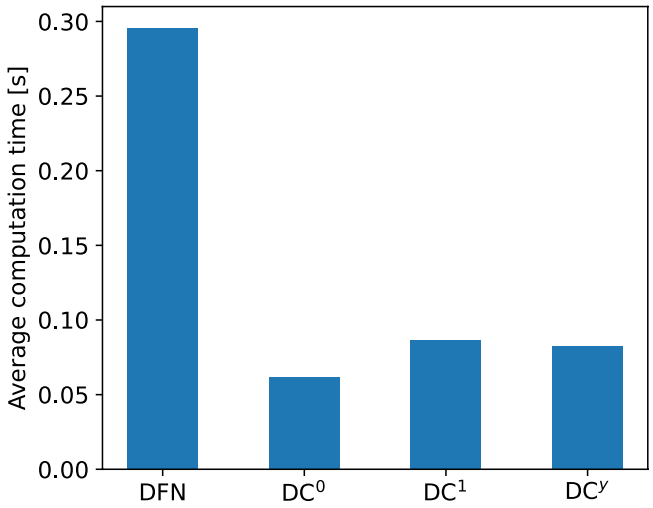

Figure 7. The computation time for each model averaged across the four electrodes.

each model as similar as possible—effective properties are identical, material properties are taken directly from the DNS parameter set, and the same length scale is used for DFN and DC^{y}.

Computation time.—The total computation time was compared for the simulations above, with results shown in Fig. 7 (see the SM for more details on the calculations). The absolute time taken for each simulation is not of interest, since this depends heavily on the system used and the numerical approach, but rather the time relative to other models. The DC models require between 70% and 80% less computation time than the DFN. This is because they are genuinely 1D, compared to the (pseudo) 2D description of the DFN. Thus, for a half-cell modelled using a typical DFN with 20 nodes in the separator, 40 nodes in the positive electrode, and 20 nodes in the radial dimension, the total number of mesh nodes will be 860, compared to a mere 60 nodes for the equivalent DC model.

One potential criticism foreseen is that the DFN computation time is already only a fraction of a second, and thus reducing this further is relatively futile. However there are several applications where such a reduction in computation time is significant. Within battery management systems, where resources are limited and time requirements are strict, the DFN is widely considered too computationally heavy,[9,12] and thus more lightweight (yet still physics-based) models are desired. Likewise in parameter optimisation or ageing studies, a very large number of simulations must be completed and thus the complexity of the DFN becomes burdensome.

Validation Using Experimental Data

Knowledge of the battery microstructure is not always available, and thus the closure variable required for DC^{1} cannot be calculated as shown in the previous sections. In such a case, $\langle s \rangle_A$ can simply be treated as another parameter, and the model inputs can be optimised to accurately reproduce experimental cell-voltage data, as is routinely done for the DFN.[28,32,35,37,62] In this section, we perform a validation similar to that for Yang's DC model—both the DFN and DC model parameter sets are optimised to reduce the root-mean squared error (RMSE) between model predictions and experimental data at a certain C-rate. Then, the resulting parameter sets are tested at different C-rates.

Chen's experimental voltage data[35] is used as a reference, which was measured on a commercial cell (LGM 50) with a graphite-SiOx negative electrode and an NMC 811 positive electrode. For the DFN, the degrees of freedom in the optimisation problem are identical to those chosen by Yang, and are summarised in Table IV. The values for all parameters not shown in Table IV were taken from Chen's work.[35] Note that the parameter sets are the exact same size for the two models, since there are 4 parameters that appear in the DFN that do not appear in DC^{1}, and vice versa. The parameterisation was performed using the discharge data at 1C, and the parameter sets were then validated using experimental data at 0.5C and 1.5C. Scipy's Differential Evolution algorithm was used with the following cost function,

$$\text{RMSE} = \sqrt{\frac{1}{n}\sum_{i=1}^{n}\left(V_{\text{exp}} - V_{\text{model}}\right)^2}\,, \qquad [56]$$

where n is the number of data points, whilst V_{exp} and V_{model} are the experimental and model voltage readings respectively. During the optimisation procedure, certain extreme parameter inputs may be trialled, causing models to fail—in such cases, a high RMSE value was returned to penalise the trialled parameter set.

For the optimisation at 1C, the resulting parameter sets for both models are shown in Table IV, and the cell-voltage profiles are shown in Fig. 8. For the 1C discharge rate, both models have a similar prediction accuracy, and are able to recreate the experimental voltage measurements well; this is unsurprising, as the optimisation was performed using this data. However, at both other discharge rates, the models capture the experimental discharge well. What's more, DC^{1} shows a slight improvement in accuracy compared to the DFN, especially at 1.5C.

Table IV. The optimised parameter sets for DFN and DC^{1}.

Parameter	DFN	DC^{1}
Initial concentration in negative electrode [mol·m^{-3}]	29541.5	29901.3
Initial concentration in positive electrode [mol·m^{-3}]	16842.2	18051.3
Maximum concentration in negative electrode [mol·m^{-3}]	32694.2	33304.8
Maximum concentration in positive electrode [mol·m^{-3}]	62266.0	57399.3
Negative electrode reaction-rate constant [Am^{-2}(m^{3}mol^{-1})$^{1.5}$]	4.908×10^{-7}	9.480×10^{-7}
Positive electrode reaction-rate constant [Am^{-2}(m^{3}mol^{-1})$^{1.5}$]	4.414×10^{-6}	2.053×10^{-6}
Negative electrode tortuosity (electrolyte)	2.738	2.735
Positive electrode tortuosity (electrolyte)	2.802	1.944
Negative electrode diffusivity [m^{2}s^{-1}]	1.332×10^{-13}	—
Positive electrode diffusivity [m^{2}s^{-1}]	5.126×10^{-15}	—
Negative particle radius [m]	6.401×10^{-6}	—
Positive particle radius [m]	5.266×10^{-6}	—
Negative electrode specific surface area [m^{-1}]	—	441818.3
Positive electrode specific surface area [m^{-1}]	—	412729.1
Negative electrode $\langle s \rangle_A$ [mol·m^{-1}A^{-1}]	—	−335.06
Positive electrode $\langle s \rangle_A$ [mol·m^{-1}A^{-1}]	—	−500.38

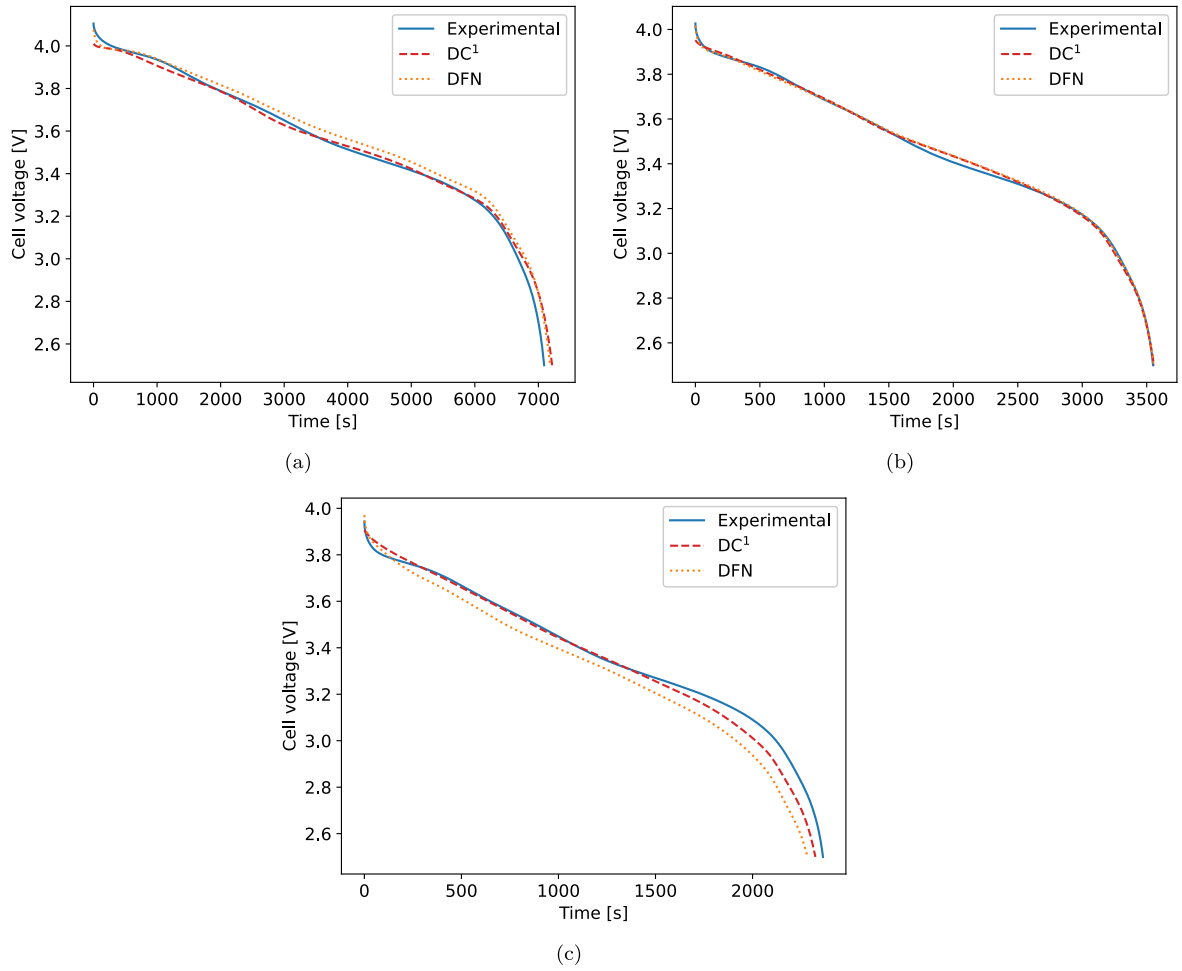

Figure 8. Experimental cell-voltage readings alongside the DFN and DC[1] predictions for 0.5C (a), 1C (b), and 1.5C (c).

Conclusions

In this work, we employed the volume-averaging technique to develop a dual-continuum (DC) model that incorporates a closure problem to capture the influence of electrode microstructure on mass transport within active material (AM) particles. From this closure, we derived an estimate of AM surface concentration, enabling a more accurate calculation of the reaction rate. Importantly, the closure depends solely on the microstructure and is independent of material properties or operating conditions.

We first validated the DC model against a detailed microscale model by simulating four 2D electrode structures and a 3D electrode reconstructed from tomographic imaging. In this validation, the ubiquitous Doyle–Fuller–Newman (DFN) model[1] and another DC model recently published by Yang and Tartakovsky[28] were also included. The electrodes were chosen so as to highlight difficulties encountered in the DFN model—namely, non-spherical particles, an ambiguous definition of particle radius, and a large particle size distribution. We then parameterised the DC model and compared its predictions with experimental cell-voltage data. For all electrodes considered, our DC model reproduced cell voltage more accurately than the DFN model while requiring 70–80% less computation time. This work also serves as further validation of Yang and Tartakovsky's DC model, since only a single microstructure was simulated in the original publication. Their model was found to be more accurate and faster than the DFN in all cases.

The volume-averaging technique used in our derivation gives physical insight into important assumptions made in the DC model. In Part II, we revisit the derivation, and propose four extensions to the model.

Acknowledgments

The authors gratefully acknowledge financial support from TotalEnergies, whose collaboration was instrumental in enabling this research.

ORCID

Isaac B. Paten https://orcid.org/0009-0007-2720-4969
Martin Petitfrére https://orcid.org/0009-0004-8489-1548
Céline Merlet https://orcid.org/0000-0003-3758-273X
Romain De Loubens https://orcid.org/0009-0008-6474-9324
Michel Quintard https://orcid.org/0000-0002-6150-7011
Yohan Davit https://orcid.org/0000-0002-2234-9567

References

1. M. Doyle, T. F. Fuller, and J. Newman, "Modeling of galvanostatic charge and discharge of the lithium/polymer/insertion cell." *J. Electrochem. Soc.*, **140**, 1526 (1993).
2. G. Richardson, I. Korotkin, R. Ranom, M. Castle, and J. M. Foster, "Generalised single particle models for high-rate operation of graded lithium-ion electrodes: Systematic derivation and validation." *Electrochimica Acta*, **339**, 135862 (2020).
3. S. G. Marquis, V. Sulzer, R. Timms, C. P. Please, and S. J. Chapman, "An asymptotic derivation of a single particle model with electrolyte." *J. Electrochem. Soc.*, **166**, A3693 (2019).
4. V. R. Subramanian, V. D. Diwakar, and D. Tapriyal, "Efficient macro-micro scale coupled modeling of batteries." *J. Electrochem. Soc.*, **152**, A2002 (2005).
5. V. R. Subramanian, V. Boovaragavan, and V. D. Diwakar, "Toward real-time simulation of physics based lithium-ion battery models." *Electrochemical and Solid-StateLetters*, **10**, A255 (2007).

6. Y. Davit et al., "Homogenization via formal multiscale asymptotics and volume averaging: How do the two techniques compare?" *Advances in Water Resources*, **62**, 178 (2013).
7. S. Whitaker, "Diffusion and heterogeneous reaction in porous media." *The Method of Volume Averaging* 1 (Springer Netherlands, Dordrecht) (1999), 10.1007/978-94-017-3389-2_1.
8. Y. Davit and M. Quintard, "Theoretical analysis of transport in porous media: Multi-equation and hybrid models for a generic transport problem with nonlinear source terms." *Handbook of Porous Media, Third Edition* (CRC Press, Boca Raton) 3rd ed. 245 (2015), 10.1201/b18614.
9. F. Brosa Planella et al., "A continuum of physics-based lithium-ion battery models reviewed." *Progress in Energy*, **4**, 042003 (2022).
10. D. Lasseux, F. J. Valdés-Parada, and F. Bellet, "Macroscopic model for unsteady flow in porous media." *J. Fluid Mech.*, **862**, 283 (2019).
11. G. Lenne, E. Woillez, and M. Chandesris, "Modeling of Li-ion battery electrodes accounting for microstructure properties: The Newman's model revisited." *J. Electrochem. Soc.*, **171**, 70507 (2024).
12. L. Gregory, "Plett." *Battery Management Systems* Vol. 1 (Artech House, Norwood, MA) 97863081 (2015).
13. F. J. Méndez-Corbacho, Beñat Larrarte-Lizarralde, Rubén Parra, J. Larrain, D. del Olmo, Hans-Jürgen Grande, and E. Ayerbe, "Physics-informed neural networks for modeling Li-ion batteries: Solving the single particle model without labeled data." *J. Electrochem. Soc.*, **171**, 110534 (2024).
14. S. Liu, "An analytical solution to Li/Li^+ insertion into a porous electrode." *Solid State Ionics*, **177**, 53 (2006).
15. C. Y. Wang, W. B. Gu, and B. Y. Liaw, "Micro-macroscopic coupled modeling of batteries and fuel cells: I. Model development." *J. Electrochem. Soc.*, **145**, 3407 (1998).
16. W. B. Gu, C. Y. Wang, and B. Y. Liaw, "Micro-macroscopic coupled modeling of batteries and fuel cells: II. Application to nickel-cadmium and nickel-metal hydride cells." *J. Electrochem. Soc.*, **145**, 3418 (1998).
17. Q. Zhang and R. E. White, "Comparison of approximate solution methods for the solid phase diffusion equation in a porous electrode model." *Journal of Power Sources*, **165**, 880 (2007).
18. V. R. Subramanian, V. Boovaragavan, V. Ramadesigan, and M. Arabandi, "Mathematical model reformulation for lithium-Ion battery simulations: Galvanostatic boundary conditions." *J. Electrochem. Soc.*, **156**, A260 (2009).
19. V. Ramadesigan, V. Boovaragavan, J. C. Pirkle, and V. R. Subramanian, "Efficient reformulation of solid-phase diffusion in physics-based lithium-ion battery models." *J. Electrochem. Soc.*, **157**, A854 (2010).
20. K. Chayambuka, G. Mulder, D. L. Danilov, and P. H. L. Notten, "A modified pseudo-steady-state analytical expression for battery modeling." *Solid State Commun.*, **296**, 49 (2019).
21. T. F. Fuller, M. Doyle, and J. Newman, "Simulation and optimization of the dual lithium ion insertion cell." *J. Electrochem. Soc.*, **141**, 1 (1994).
22. M. Guo, X. Jin, and R. E. White, "Nonlinear state-variable method for solving physics-based Li-ion cell model with high-frequency inputs." *J. Electrochem. Soc.*, **164**, E3001 (2017).
23. I. R. Moyles, M. G. Hennessy, T. G. Myers, and B. R. Wetton, "Asymptotic reduction of a porous electrode model for lithium-ion batteries." *SIAM J. Appl. Math.*, **79**, 1528 (2019).
24. M. Quintard and S. Whitaker, "One- and two-equation models for transient diffusion processes in two-phase systems." *Advances in Heat Transfer* (Elsevier) Vol. 23, 369 (1993), 10.1016/S0065-2717(08)70009-1.
25. L. Li, H. Zhou, and J. J. Gómez-Hernández, "Transport upscaling using multi-rate mass transfer in three-dimensional highly heterogeneous porous media." *Advances in Water Resources*, **34**, 478 (2011).
26. O. Silva, J. Carrera, M. Dentz, S. Kumar, A. Alcolea, and M. Willmann, "A general real-time formulation for multi-rate mass transfer problems." *Hydrology and Earth System Sciences*, **13**, 1399 (2009).
27. H. H. Gerke and M. T. van Genuchten, "A dual-porosity model for simulating the preferential movement of water and solutes in structured porous media." *Water Resources Research*, **29**, 305 (1993).
28. X. Yang and D. M. Tartakovsky, "Dual-cContinuum models of electrochemical transport in porous electrodes." *J. Electrochem. Soc.*, **172**, 20507 (2025).
29. J. Guo, M. Quintard, and F. Laouafa, "Dispersion in porous media with heterogeneous nonlinear reactions." *Transport in Porous Media*, **109**, 541 (2015).
30. P. Landereau, B. Noetinger, and M. Quintard, "Quasi-steady two-equation models for diffusive transport in fractured porous media: Large-scale properties for densely fractured systems." *Advances in Water Resources*, **24**, 863 (2001).
31. F. Douarche, B. Braconnier, S. Momeni, M. Quintard, and B. Nœtinger, "Counter-current imbibition and non-linear diffusion in fractured porous media: Analysis of early- and late-time regimes and application to inter-porosity flux." *Advances in Water Resources*, **169**, 104319 (2022).
32. H. Arunachalam and S. Onori, "Full homogenized macroscale model and pseudo-2-dimensional model for lithium-ion battery dynamics: Comparative analysis, experimental verification and sensitivity analysis." *J. Electrochem. Soc.*, **166**, A1380 (2019).
33. P. Mohtat, S. Lee, V. Sulzer, J. B. Siegel, and A. G. Stefanopoulou, "Differential expansion and voltage model for Li-ion batteries at practical charging rates." *J. Electrochem. Soc.*, **167**, 110561 (2020).
34. S. Hein et al., "Influence of conductive additives and binder on the impedance of lithium-ion battery electrodes: Effect of morphology." *J. Electrochem. Soc.*, **167**, 013546 (2020).
35. C.-H. Chen, F. Brosa Planella, K. O'Regan, D. Gastol, W. D. Widanage, and E. Kendrick, "Development of experimental techniques for parameterization of multi-scale lithium-ion battery models." *J. Electrochem. Soc.*, **167**, 080534 (2020).
36. S. Lea, A. Kremer, T. Hoffmann, S. Danner, B. Hein, D. Prifling, C. Westhoff, A. Dreer, V. Latz, and M. Schmidt, "Wohlfahrt-Mehrens. Manufacturing process for improved ultra-thick cathodes in high-energy lithium-ion batteries." *Energy Technology*, **8**, 1900167 (2020).
37. E. C. Tredenick, A. M. Boyce, S. Wheeler, J. Li, Y. Sun, R. Drummond, S. R. Duncan, P. S. Grant, and P. R. Shearing, "Bridging the gap between microstructurally resolved computed tomography-based and homogenised Doyle-Fuller-Newman models for lithium-ion batteries." *J. Electrochem. Soc.*, **172**, 030503 (2025).
38. A. Schmidt, E. Ramani, T. Carraro, J. Joos, André Weber, M. Kamlah, and E. Ivers-Tiffée, "Understanding deviations between spatially resolved and homogenized cathode models of lithium-ion batteries." *Energy Technology*, **9**, 20008812194 (2021).
39. G. M. Goldin, A. M. Colclasure, A. H. Wiedemann, and R. J. Kee, "Three-dimensional particle-resolved models of Li-ion batteries to assist the evaluation of empirical parameters in one-dimensional models." *Electrochimica Acta*, **64**, 118 (2012).
40. A. M. Boyce, X. Lu, D. J. L. Brett, and P. R. Shearing, "Exploring the influence of porosity and thickness on lithium-ion battery electrodes using an image-based model." *Journal of Power Sources*, **542**, 231779 (2022).
41. M. Quintard and S. Whitaker, "Transport in ordered and disordered porous media: I. The cellular average and the use of weighting functions." *Transport in Porous Media*, **14**, 163 (1994).
42. M. Quintard and S. Whitaker, "Transport in ordered and disordered porous media: II. Generalized volume averaging." *Transport in Porous Media*, **14**, 179 (1994).
43. Y. Davit and M. Quintard, "Technical notes on volume averaging in porous media: I. How to choose a spatial averaging operator for periodic and quasiperiodic structures." *Transport in Porous Media*, **119**, 555 (2017).
44. M. J. Hunt, F. Brosa Planella, F. Theil, and W. D. Widanage, "Derivation of an effective thermal electrochemical model for porous electrode batteries using asymptotic homogenisation." *Journal of Engineering Mathematics*, **122**, 31 (2020).
45. Y. Nomura, K. Yamamoto, T. Hirayama, E. Igaki, and K. Saitoh, "Visualization of lithium transfer resistance in secondary particle cathodes of bulk-type solid-state batteries." *ACS Energy Lett.*, **5**, 2098 (2020).
46. Y. Davit, F. Golfier, J.-C. Latché, and M. Quintard, "A domain decomposition approach to finite-epsilon homogenization of scalar transport in porous media." *SIAM Journal on Applied Mathematics*, **79**, 1797 (2019).
47. F. L. E. Usseglio-Viretta et al., "Resolving the discrepancy in tortuosity factor estimation for Li-ion battery electrodes through micro-macro modeling and experiment." *J. Electrochem. Soc.*, **165**, A3403 (2018).
48. G. B. Less, J. H. Seo, S. Han, A. M. Sastry, J. Zausch, A. Latz, S. Schmidt, C. Wieser, D. Kehrwald, and S. Fell, "Micro-scale modeling of Li-ion batteries: Parameterization and validation." *J. Electrochem. Soc.*, **159**, A697 (2012).
49. A. Latz and J. Zausch, "Thermodynamic consistent transport theory of Li-ion batteries." *Journal of Power Sources*, **196**, 3296 (2011).
50. (2024), COMSOL Multiphysics Lithium-Ion Battery Module, COMSOL AB.
51. V. Sulzer, S. G. Marquis, R. Timms, M. Robinson, and S. J. Chapman, "Python battery mathematical modelling (PyBaMM)." *Journal of Open Research Software*, **9**, 14 (2021).
52. S. J. Cooper, A. Bertei, P. R. Shearing, J. A. Kilner, and N. P. Brandon, "TauFactor: An open-source application for calculating tortuosity factors from tomographic data." *SoftwareX*, **5**, 203 (2016).
53. D. Kehrwald, P. R. Shearing, N. P. Brandon, P. K. Sinha, and S. J. Harris, "Local tortuosity inhomogeneities in a lithium battery composite electrode." *J. Electrochem. Soc.*, **158**, A1393 (2011).
54. I. Paten, *Solveclosure* (2025).
55. M. Kfoury, R. Ababou, B. Noetinger, and M. Quintard, "Upscaling fractured heterogeneous media: Permeability and mass exchange coefficient." *Journal of Applied Mechanics*, **73**, 41 (2005).
56. M. Quintard, M. Kaviany, and S. Whitaker, "Two-medium treatment of heat transfer in porous media: Numerical results for effective properties." *Advances in Water Resources*, **20**, 77 (1997).
57. M. Ahmed-Maloum, T. David, L. Guetaz, P. Duru, Joël Pauchet, M. Quintard, and M. Prat, "Computation of oxygen diffusion properties of the gas diffusion medium -microporous layer assembly from the combination of X-ray microtomography and focused ion beam three dimensional digital images." *Journal of Power Sources*, **561**, 232735 (2023).
58. L. O. Valoen and J. N. Reimers, "Transport Properties of LiPF[sub 6]-Based Li-Ion Battery Electrolytes." *J. Electrochem. Soc.*, **152**, A882 (2005).
59. M. F. Lagadec, R. Zahn, and V. Wood, "Characterization and performance evaluation of lithium-ion battery separators." *Nat. Energy*, **4**, 16 (2018).
60. T. L. Kirk, C. P. Please, and S. Jon Chapman, "Physical modelling of the slow voltage relaxation phenomenon in lithium-ion batteries." *J. Electrochem. Soc.*, **168**, 060554 (2021).
61. T. Danner, M. Singh, S. Hein, Jörg Kaiser, H. Hahn, and A. Latz, "Thick electrodes for Li-ion batteries: A model based analysis." *Journal of Power Sources*, **334**, 191 (2016).
62. M. Ecker, T. K. D. Tran, P. Dechent, S. Käbitz, A. Warnecke, and D. U. Sauer, "Parameterization of a physico-chemical model of a lithium-ion battery: I. Determination of parameters." *J. Electrochem. Soc.*, **162**, A1836 (2015).